Ion beam synthesis of buried Zn-VI quantum dots in SiO_2 – grazing incidence small-angle X-ray scattering studies

I.D. Desnica-Frankovic,[a*] U.V. Desnica,[a] P. Dubcek,[a] M. Buljan,[a] S. Bernstorff,[b] H. Karl,[c] I. Grosshans[c] and B. Stritzker[c]

[a]R. Boskovic Institute, PO Box 180, 10000 Zagreb, Croatia, [b]Sincrotrone Trieste, SS 14 km163.5, 34012 Basovizza, Italy, and [c]Institut für Physik, Universität Augsburg, Universitätsstr. 1, D-86135 Augsburg, Germany. E-mail: dunja.desnica@irb.hr

Grazing incidence small angle X-ray scattering was used to study ion-beam synthesized Zn-VI compound-semiconductor quantum dots (QDs), buried in a SiO_2 matrix. The ZnTe and ZnS QDs were formed by successive ion implantation of constituent atoms, at high ion doses and subsequent annealing at different temperatures in the 1073–1373 K range. In Zn and Te implanted SiO_2, small nano-crystals were formed At higher annealing-temperatures, a bimodal size distribution of nano-particles was observed for both materials, which could be explained by an interplay of Ostwald ripening and enhanced diffusion in the irradiation-damaged region.

Keywords: grazing incidence, small angle x-ray scattering, ion implantation, nano-particles, quantum dots, ZnS, ZnTe

1. Introduction

The discovery that nano-structures exhibit a variety of new and fascinating properties, completely different from their bulk analogues, offering a vast number of potential applications, has prompted a worldwide frenzy in studying various structures within nano-metric dimensions. Out of the gallery of nano-sized species, semiconductor quantum-size particles, quantum dots (QDs), show strong visible luminescence and pronounced effects of quantum confinement resulting in an increase of the energy bandgap. One of the important methods for QD synthesis is ion implantation in an appropriate matrix (White *et al*., 1999; Budai *et al*., 1997; Meldrum *et al.*, 1999). During implantation and a possible subsequent thermal annealing procedure, the implanted material precipitates in a thin buried layer. Since essential physical properties depend on the characteristics of the ensemble of the QDs, those properties could, in principle, be optimized for a particular application by controlling the concentration and the size of precipitated QDs. Ion implantation allows control over the profile of implanted ions i.e. the initial supersaturation and therefore the position, size-distribution and density of the precipitated phase. However, a number of problems is still blocking the successful commercial implementation of ion-beam synthesis of semiconductor QDs, such as relatively wide particle size distributions, or the radiation-induced defects and structural modifications, that occur in the host matrix during implantation, which afterwards serve as nucleation sites in the process of growth of the precipitates. In this paper we are presenting our studies on nucleation and growth of ZnS and ZnTe QDs formed by implantation of energetic ions in thermal SiO_2. We have employed grazing incidence small angle X-ray scattering (GISAXS) and cross-sectional transmission electron microscopy (XTEM) images to analyze the influence of implantation parameters and various post-implantation thermal treatments on the QDs' size and size distributions.

2. Experimental

Two types of samples were produced. In one series equal doses ($4x10^{16}/cm^2$) of Te and Zn ions were implanted into the 300-nm thick thermally grown SiO_2 on (100)-silicon at room temperature (RT). The ion beam energies (115 keV ^{68}Zn, 190 keV ^{130}Te) were selected to obtain a projected range of approximately 80 nm for both elements. The Te ions were implanted first, followed by implantation of Zn ions. The samples were subsequently annealed in a rapid-thermal-processing furnace at T_{a1} = 1073 K for 16 min, at T_{a2} = 1273 K for 30 s and T_{a3} = 1273 K for 16 min, in the flow of Ar+ 4% H_2 at atmospheric pressure. A second series of samples was obtained by multienergy implantation of S and Zn ions, to secure a uniform concentration profile along the implanted part of the 1 µm thick thermally grown SiO_2 on (100) Si. The total dose was $7.6x10^{16}$ $/cm^2$ and the thermal processing conditions were T_{a1} = 1173 K, 30 min; T_{a2} = 1273 K, 30 min and T_{a3} = 1373 K, 15min.

GISAXS experiments were carried out at the SAXS-beamline (Amenitsch et al, 1997) of the Elettra synchrotron radiation facility in Trieste, Italy. The employed X-ray wavelength was λ = 0.154 nm. GISAXS patterns were recorded with a two-dimensional CCD-detector containing 1024x1024 pixels, placed perpendicular to the incident beam. A thin Al-stripe was placed in front of the 2D detector in order to attenuate the very intense specular reflected beam and thus avoid overflow of the detector. Spectra were corrected for background intensity and detector response, and then for refraction and absorption effects ((Kutsch *et al*., 1997; Buljan *et al*., 2002). For each sample the GISAXS pattern was first recorded at the angle of incidence, α_i, equal to the critical angle for total external reflection, α_c, when the refracted wave propagates quasi-parallel just under the surface. The angle of incidence angle was then systematically increased in order to probe deeper parts of the layer and thus perform the depth distribution profiling.

3. Results

3.1. ZnS nanoparticles

The 2D GISAXS pattern, at the angle of incidence $\alpha_i = \alpha_c+0.05^o$, of a Zn and S implanted sample, annealed at 1173 K for 30 min is shown in the Fig 1*a*. This α_i corresponds to the X-ray penetration depth of l=310 nm calculated from the expression $l = 1/|\mathrm{Im}\, k_z|$ where k_z is the vertical component of the incident

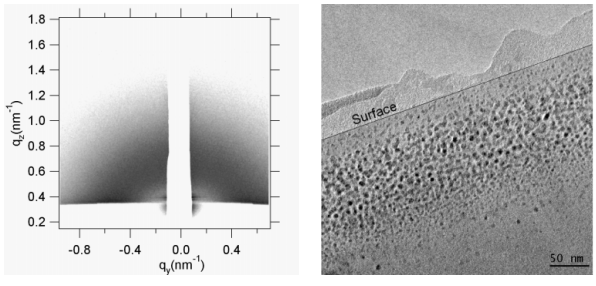

Figure 1

Two-dimensional GISAXS pattern of the Zn and S implanted sample taken at the incidence angle $\alpha_i = \alpha_c+0.05^o$: (*a*) annealed for 30 min at 1173 K, the interference maximum represented by a half-ring, is related to the spatial correlation between isolated nanoparticles. (*b*) cross-sectional TEM image for the analogous sample.

wave vector in the substrate (Vineyard, 1982; Raucher *et al.*, 1999). Since the projected range for both implanted elements is approximately 80 nm, in this arrangement, most of the implanted layer is being probed. The most prominent feature in the GISAXS pattern is the presence of a well defined half-ring, which is considered as due to scattering at nanoparticles embedded in the SiO_2 matrix. The almost spherical shape indicates an isotropic distribution of QDs formed after the 1173 K annealing. The corresponding scattering intensity profile obtained as a cross section parallel to the q_z axis, where q_z is the z-component of the wave vector $\boldsymbol{q}$ [with $q = (4\pi/\lambda)\sin\theta$; 2θ is the scattering angle], is depicted in Fig. 2, curve (*a*).

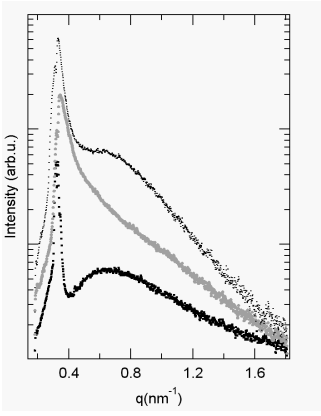

Figure 2

1D cross-sections of GISAXS patterns of Fig. 1, cut parallel to q_z. Curve (*a*)-black thick line, corresponds to the sample annealed at T_a = 1173 K, t_a = 30 min; (b)-grey line, at T_a = 1273 K, t_a = 30 min; (*c*)-black thin line, at T_a = 1373 K, t_a = 15 min. The curves are vertically offset for clarity.

The plot is essentially characterized by two contributions: by a strong small angle signal at the lower q values arising from the surface effects, including surface roughness and a Yoneda peak, and by the presence of an interference maximum at higher q values, due to the scattering on nanoparticles. The maximum indicates spatial correlation between QDs. From the position of the maximum, q_{max}, by applying a simple Guinier-plot analysis (Guinier&Fourner, 1955), a correlation length $\Lambda = 2\pi/q_{max}$ = 9.1 nm is obtained. In addition, from the slope of the linear part of the ln $I(q)$ *vs.* q^2 dependence for $q > q_{max}$, we have calculated the Guinier radius of QDs as r_G=2.3 nm. A predominantly spherical shape of the clusters was deduced from the analysis of scattering intensity profiles taken at various polar angles. These findings are consistent with the cross-sectional TEM image taken at the analogous sample (Fig. 1b).

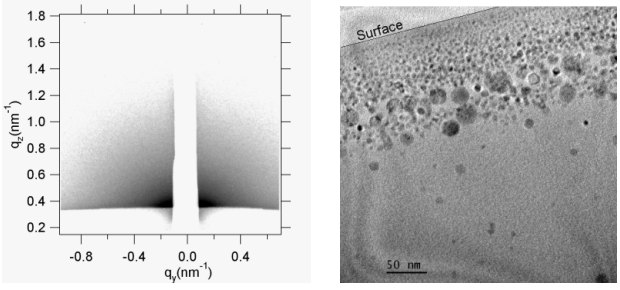

Figure 3

Two-dimensional GISAXS pattern of the Zn and S implanted sample taken at the incidence angle $\alpha_i = \alpha_c + 0.05^o$: (*a*) annealed for 30 min at 1273 K. (*b*) cross-sectional TEM image for the analogous sample.

For higher annealing temperatures, the 2D-scattering pattern changes profoundly (Fig.3*a*): for 30 min annealing at 1273 K the interference maximum disappears, the particles are less correlated, the size distribution could be very broad. Also, if larger particles with larger inter-particle distance are created, the correlation maximum could be located below the shadow of the sample, at angles smaller than the angle of incidence. Consequently, the averaged distance between nanoparticles could not be established. The strong scattering intensity near the beam-stopper is assumed to arise from the presence of a population of larger clusters. The existence of large clusters in ZnS after annealing at 1273 K for 30 min (in addition to a distribution of small ones) is also confirmed by the cross-sectional TEM image (Fig. 3*b*).

To compare the influence of the annealing procedure, the 1D profiles of the intensity map for three different annealing temperatures are presented in Fig. 2. While the annealing for 30 min at 1173 K resulted in the formation of small, correlated nanoparticles, the sample annealed for 30 min at 1273 K could be considered as an intermediate one, characterized by a very broad distribution in particle sizes and therefore, neither the particle-related interference ring, nor the shouldering could be resolved. However, after annealing at 1373 K for 15 min the precipitates have been redistributed into a set similar to the one obtained after annealing at 1173 K but of somewhat larger particles at greater distances. This is indicated by the appearance of shouldering resembling the interference ring in the curve (c). The average radius of gyration was determined from the regions at small q, in the interval from q=0.75 nm to q=1.4 nm, where the linear relation of ln I(q) vs. q^2 is satisfied [Fig.2, curves (*a*), (*b*) and (*c*)]. The obtained values were: $R_{g,1173}$= 2.3 nm, $R_{g,1273}$= 2.54 nm, and $R_{g,1373}$= 2.9 nm, and correspond to the mean value for both populations of nanoclusters.

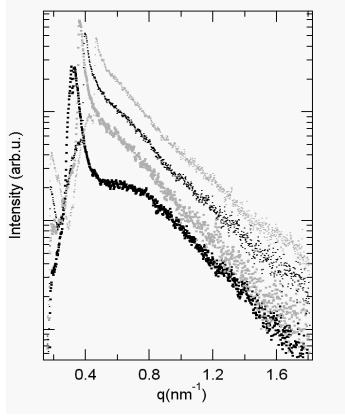

Figure 4

Cross-sections of GISAXS patterns for the Zn and S -implanted sample annealed for 15 min at 1373 K. (*a*)-black thick line: $\alpha_i = \alpha_c$, (*b*)-gray thick line: $\alpha_i = \alpha_c + 0.05^o$, (*c*)-black thin line: $\alpha_i = \alpha_c + 0.1^o$, (*d*)-gray thin line: $\alpha_i = \alpha_c + 0.2^o$. The curves are vertically offset for clarity.

To analyze the implanted layer along the direction perpendicular to the surface, the incident angle was systematically increased from $\alpha_i = \alpha_c$ to $\alpha_i = \alpha_c + 0.2^o$. These angles corresponded to an average penetration depth of 36, 310, 450 and 674 nm, respectively. Thus, a much deeper section of the sample than the projected range of implanted ions was probed. The results, obtained on a sample annealed 15 min at 1373 K, are depicted in Fig. 4. Pronounced shouldering is present only for $\alpha_i = \alpha_c$ (curve *a*), indicating spatial correlation between QDs within the layer solely in the region immediately beneath the surface. As the incidence angle is being increased, the scattering profile is composed of contributions from deeper parts of the layer. This scattering pattern could be interpreted

as the result of superposition of contributions coming from two populations of clusters with different size distributions within the implanted layer. To further explore this option, the spectra were analyzed by the local monodisperse aproximation, LMA, which includes the structure factor and polydispersity of the system (Pedersen, 1994; Rauscher *et al.*,1995; Cattaruzza *et al.*, 2000). Within this approximation the scattering intensity in GISAXS spectra is expressed by

$$I(q) \propto \left|T(\alpha_i)\right|^2 \left|T(\alpha_f)\right|^2 \int_0^\infty F(q,R)S(q,R_{HS},\eta_{HS})G(R,w) \quad (1)$$

where $T(\alpha_i)$ and $T(\alpha_f)$ are the Fresnel transmission coefficients for the angle of incidence and exit, respectively. The $F(q, R)$, $S(q, R_{HS}, \eta_{HS})$, and η_{HS} are the form factor of a homogeneous sphere of radius R, the structure factor of the assembly, and the volume fraction of the hard spheres, respectively. $G(R,w)$ is the Gaussian size distribution function, specified by its width parameter w, $G(R,w) = \frac{1}{\sqrt{2\pi}w} e^{\frac{-(R-R_0)^2}{2w^2}}$. From the fit we have found that a shallow sub-surface layer (less than 30 nm) is populated by QDs of average R_{LMA} = 2.4 nm, with size distribution characterized by w = 0.68 nm. As the incidence angle was increased to $\alpha_i = \alpha_c + 0.05^o$, the penetration increased to 300 nm, and in addition to the distribution of QDs with R_{LMA1} = 2.9 nm, a second distribution of much bigger nanoparticles was revealed with a mean radius centered at R_{LMA2} = 9 nm. The size distribution parameters w_1 = 1.5 nm and w_2 = 1.9 nm respectively, were obtained. When probing deeper into the layer, the relative concentration (obtained as a parameter from the LMA fit) of bigger QDs, increases from very small fraction of 0.2% at $\alpha_i=\alpha_c+0.02^o$ to 1.6% at $\alpha_i=\alpha_c+0.1^o$. Several authors already demonstrated the occurrence of two different size distributions of precipitates of II-VI compounds implanted in a light matrix. For instance, Bonafos et al. (1999) have evidenced two separate bands of particles for ion-beam synthesized ZnS-QDs in SiO_2 after the 1373 K-annealings by cross-sectional TEM. The spatial self-structuring, evoked to explain the GISAXS scattering profiles, was already confirmed in a number of semiconductor-QDs systems (Meldrum *et al.*, 2001). Additional support also comes from elaborate computer simulations done by Reiss and Heinig (Reiss&Heinig, 1994; 1996) who have shown that spatial redistribution of growing nanoparticles is the effect of pure Ostwald ripening when appropriate initial conditions are met. Furthermore, it was found that in some ion-beam synthesized II-VI compounds (Bonafos *et al.*, 1999) the size distributions of nanoclusters are centered in the vicinity of the end-of-range positions for respective implanted ions. Since the end-of-range region for the particular implanted ions is characterized by a peak of damage received by the substrate upon implantation, the self-organization of precipitates could be considered as a consequence of the heterogeneous nucleation of precipitates preferentially centered in the two most damaged areas. Moreover, an additional contribution to the scattering intensity at small q-s due to scattering from a rough internal quasi-interface, especially at larger incidence angles, is also not excluded, since it was established (TEM, Fig. 3*b*) that there is an abrupt change from the densely precipitated ZnS-phase region to the 'empty' SiO_2.

3.2. ZnTe nanocrystals

In the Zn and Te -implanted SiO_2-samples the synthesis of nanoclusters begins already during implantation, giving rise to the scattering *(a)* in Fig. 5. Small nanoclusters are spatially correlated, with average radius R_g = 3.3 nm and an average interparticle distance of $\Lambda \approx 8$ nm throughout the layer. Neither R_g nor Λ change much with depth, as the interference maximum retains its position in q (not shown). The annealing at 1073 K for 16 min introduces just slight changes in the scattering profile *(b)*. The results of depth probing of the sample by employing Guinier analysis have shown minor changes with depth. The obtained values were: R_{g1} = 3.4 nm, Λ_{g1} = 8,7 nm; R_{g2} =3.5 nm, Λ_{g2} = 9.4 nm; R_{g3}=3.5 nm, Λ_{g3} = 9.6 nm; R_{g4} = 3.6 nm, Λ_{g4} = 9.7 nm; for penetration lengths of 30, 154, 230 and 350 nm, respectively.

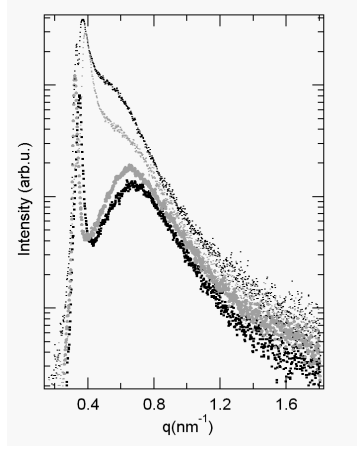

Figure 5

1D cross-sections of GISAXS patterns for the Zn and Te -implanted samples, cut parallel to q_z. Curve (*a*) -black thick line- corresponds to the as-implanted sample; (*b*) -gray thick line- annealed at T_a = 1073 K, t_a = 16 min; (*c*) -black thin line- at T_a = 1273 K, t_a = 30 s; (*d*) -gray thin line- at T_a = 1273 K, t_a = 16 min. The curves are vertically offset for clarity.

However, after just 30 s annealing at 1273 K the implanted sample changes dramatically: the correlation is lost, only weak shouldering is now present at the previous position of the interference maximum (curve *c*). A similar scattering profile is obtained after 16 min annealing at 1273 K (curve *d*). From the linear parts of the plot of ln (I(q)) *vs.* q^2 the average mean radius R_g was estimated, showing a steady increase from 3.3 nm, 3.4 nm, 3.8 nm up to 4.4 nm, with annealing temperature and time.

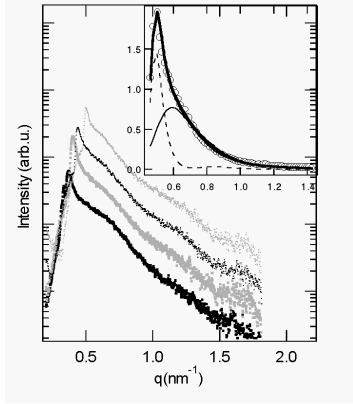

Figure 6

Cross-sections of GISAXS patterns for the Zn and Te -implanted sample annealed for 16 min at 1273 K. (*a*)-black thick line: $\alpha_i = \alpha_c$, (*b*)-gray thick line: $\alpha_i = \alpha_c + 0.05^o$, (*c*)-black thin line: $\alpha_i = \alpha_c + 0.1^o$, (*d*)-gray thin line: $\alpha_i = \alpha_c + 0.2^o$. The curves are vertically offset for clarity. *Inset*: the LMA fit to the 1D profile of (*c*), cut at a polar angle $\varphi=30^o$ with respect to the specular plane, together with the corresponding contributions of smaller and larger particles.

The 1D profiles parallel to the q_z axis of the 2D GISAXS signals obtained from a Zn+Te implanted sample annealed at 1273 K for 16 min are depicted in Fig. 6. The angle of incidence was varied from $\alpha_i = \alpha_c$ to $\alpha_i = \alpha_c + 0.2^o$. For $\alpha_i = \alpha_c$ and $\alpha_i = \alpha_c + 0.05^o$ the signals are interpreted as arising from agglomerated clusters with a broad size distribution, that are not spatially correlated. To obtain a good LMA fit the Weibull size distribution was introduced (Cattaruzza *et. al*., 2000). The Fig. 6 - inset depicts the LMA fit to the 1D profile cut at a polar angle $\varphi=30^o$, measured from the specular plane, together with the corresponding contributions of smaller and larger particles. The results suggest the presence of bi-modal size distributions with a maximum centered at $R_{LMA,} = 2.5$ nm for smaller particles, and the larger clusters diameter of approximately 30 nm. The size distribution is very broad with w_1=2.4 nm and w_2=9.6, respectively. It has to be mentioned that at least two concerns complicate these conclusions. First, the fit with so many parameters does not a priory yield fully reliable numerical results and, second, the contribution of larger particles is partially blocked by the shadow of the sample, thus not easily discernable. For $\alpha_i > \alpha_c+0.05^o$, the X-ray beam is probing all the way through the implanted layer and another contribution to GISAXS arising from the scattering at an internal quasi-surface becomes effective. It was demonstrated by TEM (Karl *et al.*, 2001) that for 20 min annealing at 1273 K the formation of ZnTe nanoparticles results in a very sharp interface in close vicinity to the Te end-of-range region (which is approximately 120 nm). This quasi-surface is comprised of large clusters that could effectively scatter X-rays in a manner similar to the scattering from a very rough surface and/or scattering from particles distributed along the surface. The contribution of such scattering reaches out of the specular plane and is seen at larger *q*-s as well.

4. Discussion and conclusions

By the analysis of 2D GISAXS patterns a successful ion-beam synthesis of ZnS and ZnTe quantum dots in SiO_2 samples was confirmed. In the Zn + Te -implanted samples the formation of small particles was noticed already in the as-implanted sample, indicating that the diffusion of Zn and Te atoms and their fusion into the ZnTe nanocrystals occurs already during the process of implantation itself when the implanted doses are sufficiently high. A successive thermal treatment of the implanted samples causes further growth of the particles, with the average size depending strongly on annealing time and temperature. However, various effects influence and complicate these processes resulting in a broad size distribution of QDs. In the first place, the influence of the radiation-induced damage and modifications in the host matrix must be considered. Those defects serve as nucleation sites for precipitation, implying that the distribution of the QDs could be significantly influenced by the initial damage distribution. Depending on whether the single-energy or multiple-energy implantation sequence is being used, two types of behavior are possible: In the single-energy implantation for the synthesis of compound semiconductors (as employed here for Zn + Te –samples), implanted ions produce end-of-range damaged regions at different positions, thus the spatially separated bi-modal size distribution, evoked to explain GISAXS spectra is plausible. This assumption is also supported by TEM results. In the case of multi-energy implantation, there is a wider zone of highly damaged substrate material that serves for heterogeneous nucleation and growth and the bi-modal size distribution is not necessarily spatially separated. Nevertheless, GISAXS offers evidence for two distinct size distributions present in the implanted and annealed layer. This statement is again supported by cross-sectional TEM results. Furthermore, from the theoretical simulation of the precipitation and growth of ion beam synthesized QDs it has been established that particles embedded within a solid matrix lower their formation energy by transport of matter from the smaller to larger clusters of the distribution (Reiss & Heinig, 1996). This could ultimately lead to a system of large and unwanted size distribution, since the system would consist of a number of small particles and a limited amount of big ones growing on the expense of the smaller ones. This is also in accordance with the large size distribution observed in the present study for higher annealing temperatures and longer annealing times. Thus it seems important to opt for lower annealing temperatures if smaller particles with narrower size distribution are preferred.

The study has highlighted GISAXS as a powerful technique for the characterization of semiconducting nanoparticles in the quest for better control over the size, the size distribution and spacing of nanoparticles, which would enable optimization of the desired properties of compound-semiconductors QDs and consequently the development of functional semiconductor-nanocrystal based devices.

References

Amenitsch, H., Bernstorff, S., Kriechbaum, M., Lombardo, D., Mio, H., Rappolt, M. & Laggner, P. (1997). *J. Appl. Cryst*. **30**, 872-876

Bonafos, C., Garrido, B., Lopez, M., Romano-Rodriguez, A., Gonzalez-Varona, O., Perez-Rodriguez, A, & Morante, J.R. (1998). *Appl. Phys. Lett*. **72**, 3488-3490.

Bonafos, C., Garrido, B., Lopez, M., Romano-Rodriguez, A., Gonzalez-Varona, O., Perez-Rodriguez, A,. Morante, J.R. & Rodriguez, R. (1999). *Nuc. Instr. Meth. Phys. Res.* **B 147**, 373-376.

Budai, J.D., White, C.W., Withrow, S.P., Chisholm, M.F., Zhu, J. & Zuhr, R.A. (1997). *Nature* **390**, 384-386.

Buljan, M., Salamon, K., Dubcek, P., Desnica-Frankovic, I.D., Milat, O., Bernstorff, S. & Desnica, U.V., and references therein, *Vacuum* (2002) in press.

Cattaruza, E., d'Acapito, F., Gonella, F., Longo, A., Martorana, A., Mattei, G., Maurizio, C. & Thiaudiere, D. (2000). *J. Appl. Cryst.* **33**, 740-743.

Guinier, A. & Fournet, G. (1955). *Small angle scattering of X-rays*, New York: Wiley.

Karl, H., Großhans, I., Attenberger, W., Schmid, M.. Stritzker, B.,(2001). *Nuc. Instr. Meth. Phys. Res.* **B 178**, 126-130.

Kutsch, B., Lyon, O., Schmitt, M. Mennig, M. & Scmidt, H. (1997). *J. Appl. Crystalog*. **30** 948-956.

Meldrum, A., Boatner,L.A., & White, C.W. (2001). *Nuc. Instr. Meth. Phys. Res.* **B 178**, 7-16.

Meldrum, A., Sonder, E. Zuhr, R.A. Anderson, I.M. Budai, J.D. White & C.W. Boatner, L.A. (1999). *J. Mater. Res.* **14,** 4489-44502.

Pedersen, J.S. (1994). *J. Appl. Cryst*. **27**, 595-608.

Rauscher, M., Salditt, T. & Spohn, H. (1995). *Phys. Rev.* **B 52**, 16855-16863.

Rauscher, M., Paniago, R., Metzger, H., Kovats, Z., Domke, J., Peisl, J., Pfannes, H.-D., Schulze, J.& Eisele, I. (1999) *J. Appl. Phys.* **86**, 6763-6769.

Reiss, S. & Heinig, K.H., (1994). *Nuc. Instr. Meth. Phys. Res.* **B 84,** 229-233.

Reiss, S. & Heinig, K.H. (1996). *Nuc. Instr. Meth. Phys. Res.* **B 112**, 223-227.

Vineyard, G.H. (1982). *Phys. Rev.* **B 26**, 4146-4159.

White, C.W., Meldrum, A., Budai, J.D., Withrow, S.P., Sonder, E., Zuhr, R.A., Hembree Jr., D.M., Wu, M. & Henderson, D.O. (1999). *Nuc. Instr. Meth. Phys. Res.* **B 148**, 991-996.